QUANTITATIVE FLAW CHARACTERIZATION WITH SCANNING LASER ACOUSTIC MICROSCOPY

Edward R. Generazio and Don J. Roth
National Aeronautics and Space Administration
Lewis Research Center
Cleveland, Ohio 44135

Surface roughness and diffraction are two factors that have been observed to affect the accuracy of flaw characterization with scanning laser acoustic microscopy. Inaccuracies can arise when the surface of the test sample is acoustically rough. It is shown that, in this case, Snell's law is no longer valid for determining the direction of sound propagation within the sample. This paper investigates the relationship between the direction of sound propagation within the sample, the apparent flaw depth, and the sample's surface roughness. Diffraction effects can mask the acoustic images of minute flaws and make it difficult to establish their size, depth, and other characteristics. It is shown that for Fraunhofer diffraction conditions the acoustic image of a subsurface defect corresponds to a two-dimensional Fourier transform. Transforms based on simulated flaws are used to infer the size and shape of the actual flaw.

INTRODUCTION

With the application of fracture mechanics to the design of components under stress, the ability to accurately characterize existing material flaws by nondestructive evaluation (NDE) techniques has become extremely important. Scanning laser acoustic microscopy (SLAM) has received considerable attention in recent years as a promising NDE technique (refs. 1 to 10). SLAM is generally used for identifying the approximate position, size, shape, and depth of material flaws such as inclusions, voids, and delaminations. Materials inspected by using SLAM include electronic and structural ceramics (refs. 1 and 2).

Recent efforts have been directed toward obtaining more accurate quantitative flaw characterizations from acoustic images obtained with SLAM (refs. 1,3, and 4). Inaccuracies can arise, however, when the surface of the test specimen is acoustically rough. The acoustic image of a flaw and therefore the characterization of the flaw depend on the surface roughness of the material in which the flaw resides. For example, voids of known dimensions in as-fired structural ceramic specimens with rough surfaces are difficult to detect and characterize from the acoustic image (ref. 5). Polishing the surface of the specimens to a mirrorlike finish improves the acoustic image, and the voids are readily detected and more easily characterized (ref. 5). The effect of surface roughness on the determination of flaw depth and the direction of sound propagation was examined in detail in this study.

For subsurface flaws the acoustic image often consists of a diffraction pattern rather than a facsimile image of the flaw. In this case it is especially difficult to characterize the flaws (ref. 1). Nevertheless relationships have been implied between diffraction-dominated acoustic images of flaws and their actual size and depth (refs. 1 and 4). Since minute flaws are often detectable only by their diffraction patterns, it seems appropriate to investigate in more detail the relationship between diffraction patterns and the flaws causing them.

Some diffraction theories are applicable to typical SLAM experimental configurations. In this study we investigated methods for analyzing acoustic images and demonstrated that quantitative data can be obtained from the acoustic images when the effect of sample surface roughness and diffractive scattering are included in the analysis.

The results of two closely related investigations are presented herein. The first investigation examined the effect of sample surface roughness on the sound direction within an experimental sample. The second investigation examined the relationship between diffraction-dominated acoustic images of subsurface flaws and the characterizations of these flaws. The theoretical development and description of each experimental configuration are followed by the experimental results for each investigation. A general discussion of the interrelation of the investigations is presented.

SCANNING LASER ACOUSTIC MICROSCOPY

The development and operation of the scanning laser acoustic microscope are covered in references 7 to 10. The basic SLAM configuration is shown in figure 1(a). Longitudinal sound waves are produced by a piezoelectric transducer and transmitted through a couplant (usually distilled water) to the sample. The sound is reflected and refracted at the water-sample interface (fig. 1(b)). The angle of the transmitted sound in the sample is determined by Snell's law (ref. 11):

$$\frac{\sin \theta_s}{\sin \theta_w} = \frac{V_s}{V_w} \tag{1}$$

where V_w and V_s are the sound velocity in the water and sample, respectively. The angles θ_w and θ_s are the incident and refracted angles, respectively. Upon reaching the side of the sample opposite the incident-sound source, the sound displaces the surface to produce a "dynamic ripple" (ref. 8). To observe the dynamic ripple, a laser beam is scanned over the rippling side of the sample, which has been metallized with a reflective coating or covered with a metallized polymethylmethacrylate coverslip (fig. 1(a)). The laser light, angularly modulated by the surface deformations of the dynamic ripple, is reflected to a photodetector and subsequently demodulated to produce a real-time image on a video monitor. If the sample contains scatterers such as voids, inclusions, or density variations, the sound will be scattered or attenuated. These scattered or attenuated waves may appear as amplitude variations in the dynamic ripple and therefore may be visible as amplitude variations in the real-time video acoustic image.

EFFECT OF SURFACE ROUGHNESS ON FLAW DEPTH DETERMINATION

Background

Two widely used methods for determining flaw depth by using SLAM are (1) the shadow method (ref. 6), which is used for surface flaws, and (2) the stereoscopic method (ref. 10), which is used for determining the depth of subsurface flaws. Both methods depend on prior knowledge of ultrasound direction in the sample. This direction can be determined by Snell's law.

The configuration for the shadowing technique is shown in figure 2, where the sound is strongly attenuated by a surface flaw to form a low-sound-intensity region, or shadow. The depth of the surface flaw is estimated from the angle of sound θ_s in the material sample and the length L of the shadow region. The depth d of the surface flaw is then given by

$$d = \frac{L}{\tan \theta_s} \tag{2}$$

The configuration for the stereoscopic method is shown in figure 3. Here the position X_R of the acoustic image is noted in reference to a center position X_0. The sample is then rotated 180° about the center position. The new position X_L of the acoustic image is noted again in reference to the position X_0. If the direction of sound in the material is known, the depth d of the flaw is given by

$$d = \frac{X_R - X_L}{2 \tan \theta_s} \tag{3}$$

These simple relationships are not generally applicable to the SLAM sample configuration. Errors in depth determination may arise when θ_s is inacurrately determined. Snell's law for ultrasonic waves applies to interfaces that are acoustically flat (i.e., where the sound wavelengths in both the water and the sample material are much greater than the topological variations on the surface of the sample). A typical water-ceramic interface as measured by stylus profilometry is shown in figure 4. The ceramic sample has topological variations of the order of 2 μm. At 100 MHz the sound wavelengths λ in water and in a typical ceramic sample are 14.9 and 60 μm, respectively. At these wavelengths and because of sample surface roughnesses, Snell's law is no longer applicable. An analogy can be drawn for Snell's law between optical and acoustical theory. An optically flat piece of glass refracts light according to Snell's law, but glass with a randomly rough surface (i.e., frosted) does not. The glass appears to be frosted because the incident light is refracted (scattered) into many angles at the air-glass interface. This analogy holds for acoustically flat and rough interfaces.

Experiment

To investigate the effect of surface roughness on the estimation of flaw depth, a macroscopic surface crack (channel) was constructed with optically flat microscope slides (fig. 5(a)). The channel was 2.54 cm long, 1 mm deep, and 1 mm wide. The epoxy layer was approximately 20 μm thick. The surface of the slide opposite the channel (incident-sound surface) was roughened by

polishing in three selected regions with 1-, 3-, and 15-μm diamond polishing paste. The polishing direction and regions are shown schematically in figure 5(b). The sample was examined by SLAM with $\theta_w = 16.8°$.

Results

The surface roughnesses are shown in figure 6 for the optically flat area and the areas roughened with diamond paste. The peak-to-valley surface roughnesses for the optically flat region and the regions roughened with 1-, 3-, and 15-μm diamond paste were approximately 0.04, 0.2, 1.0, and 10 μm, respectively. These regions are cited according to their roughnesses in the remainder of this discussion.

Acoustic images of the glass slide sample near the channel are shown in figure 7. The four images shown are for incident sound on the regions of 0.04-, 0.2-, 1.0-, and 10-μm surface roughness. The acoustic image intensity (gray level) as a function of horizontal position is also shown as a continuous white curve in each part of figure 7. The amplitude of the curve represents the amplitude of the sound. From figures 7(a) to (c) three distinct areas of itensity can be identified. The left-most area (solid dark area) is the inside of the channel and is unmetallized; so no sound intensity should be observed. This is also evident in the amplitude curves in the extreme left areas before the first jump in the curve. The second area is the shadow region just to the right of the solid dark area in each figure. The amplitude curves show a marked jump at the beginning of the shadow region. The noise level (image intensity) in each shadow region is relatively constant over a length L (figs. 7(a) to (c)). This length defines the length of the shadow for each surface roughness shown. To the right of the shadow region the sound (and image) intensity increases in amplitude and fluctuates rapidly. For this third area the sound has traveled a direct path through the sample relatively unperturbed by the presence of the channel. These three areas (channel edge, shadow, and right of shadow) are quite distinct for the regions of the glass sample having 0.04-, 0.2-, and 1-μm surface roughnesses. The region having a surface roughness of 10 μm, however, reveals little evidence of these three areas.

If we assumed that Snell's law is valid for these configurations, the apparent depth of the channel can be determined from figures 2 and 7(a) to (c) and equations (1) and (2). This is shown in figure 8. The apparent channel depth varied with incident-sound surface roughness. Only for the optically flat region of 0.04-μm surface roughness was the true depth of the channel obtained. By assuming that Snell's law applies over the roughened regions, we obtained an error as large as 63 percent in determining the depth of the channel. Alternatively, or more correctly, we can determine the angle θ_s through which the sound is refracted as a function of the incident-sound surface roughness by using the known channel depth and equation (2). This is also shown in figure 8. The refracted angle varied from 43° for the optically flat region of 0.04-μm surface roughness to 30° for the region of 1.0-μm surface roughness. The optically flat region was the only region that yielded a direction of sound (shear wave) propagation that was consistent with Snell's law (eq. (1)).

DIFFRACTION EFFECTS OBSERVED IN ACOUSTIC IMAGES OF FLAWS

Background

The optical Fourier transform of an obstacle or aperture can be readily observed from its diffraction pattern when the experimental configuration yields Fraunhofer diffraction conditions (refs. 12 to 14). We examined the origin of the diffraction pattern from a single slit of width a (fig. 9). A plane wave, incident from the left, was diffracted at the slit opening. A minimum in the intensity of the diffraction pattern on an image plane at a distance d from the slit occurred when (refs. 12 and 15)

$$n\lambda = a \sin \alpha \tag{4}$$

where n, λ, and θ_s are the minimum, wavelength, and angular distance between a minimum and the central maximum. For an experimental configuration the angle at which the first minimum, n = 1, occurred is given by

$$\alpha = \tan^{-1}\left(\frac{x}{d}\right) \tag{5}$$

where x is the distance between the center of the slit and the first minimum.

A single-slit aperture will yield the two-dimensional diffraction pattern shown in figure 9(a) if the Fraunhofer conditions are met (refs. 13 and 14). Fraunhofer diffraction patterns created by an aperture are similar to those for an obstacle with the same dimensions (refs. 3 and 12). A digital two-dimensional Fourier transform of a line function simulating a single slit (fig. 9(b)) is shown in figure 9(c). It is identical to the diffraction pattern of figure 9(a). The diffraction pattern for a circular aperture, first solved by Airy by 1835 (refs. 12 and 15), is more complicated than diffraction from a single slit. Airy's results indicate that for an aperture of diameter a the angle of the first minimum occurs at

$$\alpha = \sin^{-1}\left(1.22\,\frac{\lambda}{a}\right) \tag{6}$$

A digital two-dimensional Fourier transform of a circle function simulating a circular aperture (fig. 10(a)) is shown in figure 10(b). The diffraction results follow similarly for acoustic waves.

Experiment

A naturally occurring subsurface spherical void in an ordinary piece of glass (fig. 11) was used to illustrate the acoustic diffraction patterns from a spherical scatterer. The glass was ground to a thickness of approximately 4.2 mm, and both sides were polished with 50-μm aluminum oxide. The void is 380 μm in diameter and is 700 μm below the surface.

To illustrate the acoustic diffraction pattern from a line scatterer, a 23-μm-diameter tungsten wire was ground to have a flat surface so that it was semicylindrical in shape. The wire was 1 cm long and supported 300 μm below the surface of a polymethylmethacrylate slab 1.5 mm thick (fig. 12). The slab

was polished with 50-μm aluminum oxide. Both samples were examined by using SLAM.

Results

The acoustic image for the void in glass is shown in figure 13. The diffraction pattern resembles a series of concentric circles and is similar to that of the Fourier transform of a circular obstacle shown previously (fig. 10(b)). The first minimums of intensity along the vertical direction are indicated in the figure. The distance $2x$ between these minimums is 134 μm. Combining the distance between the minimums with the known depth of the void and equation (5) yielded an experimental value of 6.00° for the angular distance between the first minimum and the central maximum. This value agrees well with the theoretical value of 5.01° obtained from equation (6).

The acoustic image for the wire embedded in polymethylmethacrylate is shown in figure 14. The image resembles the Fourier transform of a line function shown in figure 9(c). The first minimums are indicated in the figure and the distance $2x$ between them is 232 μm. Combining the distance between the minimums with the depth of the wire and equation (5) yielded an experimental value of 7.02° for the angular distance between the first minimum and the center of the void. This value agrees well with the theoretical value of 7.48° obtained from equation (4).

Since the direction of sound propagation in samples with even moderate surface roughness varies considerably from that for an optically flat surface, an alternative method to determine this direction is needed. Both the polymethylmethacrylate and glass samples were metallized with a semitransparent gold film. The positions of the subsurface defects were simultaneously observed optically and acoustically (fig. 15). From the known depth d and the apparent displacement ΔX of the defect, the angle of sound propagation in the sample is

$$\theta_s = \tan^{-1}\left(\frac{\Delta X}{d}\right) \tag{7}$$

For the glass sample $\theta_s = 27°$ and corresponds to shear waves; for the polymethylmethacrylate sample $\theta_s = 31°$ and corresponds to longitudinal waves.

DISCUSSION

The apparent direction of sound propagation within the sample changed with the roughness of the surface on which the sound impinged. This was observed even for samples exhibiting topological variations of the order of 0.02 to 1.0 μm. These results indicate that Snell's law is not generally valid for determining propagation direction for samples with acoustically rough surfaces. An accurate measurement of flaw depth depends on the correct determination of the sound direction within the sample (eqs. (2) and (3)); therefore neither the shadow method nor the stereoscopic method will yield accurate flaw depths or samples with rough surfaces.

The acoustical Fourier transforms (figs. 13 and 14) are not identical to their corresponding digital two-dimensional Fourier transforms (figs. 10(b) and 9(c)). The discrepancies are due to three theoretical conditions that are not satisfied by the experimental configuration. First, neither the wire nor the void is a two-dimensional object. Hence the standard theoretical development for two-dimensional apertures does not apply. The wire defect was purposely flattened on one side in an effort to achieve an experimental system that was nearly two dimensional. A similar polymethylmethacrylate sample was produced in which a cylindrical wire was embedded. The diffraction pattern on the left side of the central maximum was not observed on the acoustic image. Only by flattening one side of the wire was the full diffraction pattern observable. This result can be extended to the case of the void. For the void the diffraction pattern on the left side of the central maximum (fig. 14) was most likely not observed because of the dimensionality of the defect and the experimental configuration. Second, the acoustic image is formed on an image plane that is not perpendicular to the direction of sound propagation. The obliqueness of this image plane must be incorporated into the diffraction theory. Third, the experimental configuration used did not result in true Fraunhofer conditions. For the sample dimensions and sound wavelengths shown herein, the diffraction patterns were observed in the transition region between Fresnel and Fraunhofer zones. As a result the phase cancellation at the minimums was incomplete and the minimums were displaced.

The acoustic image of the void shows diffraction rings that tend to be more closely packed at distances far from the central maximum. The work by Airy (refs. 12 and 15) indicates that for a circular aperture the distance between adjacent diffraction rings should decrease with distance from the central maximum. This is consistent with the experimental results. It, however, was not seen for the digital two-dimensional Fourier transform of a digitally simulated circular aperture. This discrepancy is likely to be due to the discrete nature of the digital aperture. The aperture is not a true circle but a collection of adjacent rectangular openings of various sizes. The circumference of this simulated aperture is steplike. Fourier components that would be observed if the aperture were a true circle are missing from the transform shown in figure 6(b). These missing Fourier components are needed to form the Airy disk pattern with varying ring spacing.

CONCLUSIONS

It was shown that accurate measurements of surface and subsurface flaw characteristics depend on determining the refracted sound propagation direction within the sample. The surface roughness of the experimental sample was found to have a substantial effect on the direction of refracted sound propagation. Therefore Snell's law is not generally applicable to even moderately rough samples. However, accurate depth measurements could be made when the direction of refracted sound propagation was determined experimentally. Acoustic diffraction patterns caused by subsurface flaws were shown to be directly related to two-dimensional digital Fourier transforms of objects that simulate the size and shape of subsurface flaws.

REFERENCES

1. Kessler, L.W., D.E. Yuhas, and C.L. Vorres, "Acoustic Microscopy of Ceramics," Nondestructive Evaluation: Microstructural Characterization and Reliability Strategies, O. Buck and S.M. Wolf, eds., 1980, pp. 273-287, Metallurgical Society of AIME, Warrendale, PA.

2. Kessler, L.W., and D.E. Yuhas, "Principles and Analytical Capabilities of the Scanning Laser Acoustic Microscope (SLAM)," Scanning Electron Microscopy, Vol. 1, 1978, pp. 555-560, SEM, Inc., Chicago, IL.

3. Chou, C.H., B.T. Khuri-Yakub, and G.S. Kino, "Transmission Imaging: Foward Scattering and Scatter Reconstruction," Acoustical Imaging, Vol. 9, K.Y. Wang, ed., 1980, pp. 357-377, Plenum, New York.

4. Yuhas, D.E., T.E. McGraw, and L.W. Kessler, "Scanning Laser Acoustic Microscope Visualization of Solid Inclusions in Silicon Nitrides," Proceedings of the DARPA/AFML Review of Progress in Quantitative Nondestructive Evaluation, AFWAL-TR-80-4078, 1980, pp. 683-690, Rockwell International, Thousand Oaks, CA.

5. Roth, D.J., J. Klima, J.D. Kiser, and G.Y. Baaklini, "Reliability of Detection of Voids in Structural Ceramics Using SLAM (Scanning Laser Acoustic Microscopy)," Paper presented at the Spring Meeting of the American Society for Nondestructive Testing in Washington, DC, March 11-14, 1985.

6. Yuhas, D.E., "Characterization of Surface Flaws by Means of Acoustic Microscopy," Ultrasonic Materials Characterization, NBS-SP-596, H. Berger and M. Linzer, eds., 1980, pp. 357-368, National Bureau of Standards, Washington, DC.

7. Whitman, R.L., M. Ahmed, and A. Korpel, "A Progress Report on the Laser Scanned Acoustic Camera," Acoustic Holography, Vol. 4, G. Wade, ed., 1972, pp. 11-32, Plenum, New York.

8. Kessler, L.W., P.R. Palermo, and A. Korpel, "Practical High Resolution Microscopy," Acoustic Holography, Vol. 4, G. Wade, ed., 1972, pp. 51-71, Plenum, New York.

9. Auld, B.A., R.J. Gilbert, K. Hyllested, C.G. Roberts, and D.C. Webb, "A 1.1 Ghz Scanned Acoustic Microscope," Acoustic Holography, Vol. 4, G. Wade, ed., 1972, pp. 73-96, Plenum, New York.

10. Kessler, L.W., and D.E. Yuhas, "Acoustic Microscopy - A Tutorial Review," Acoustical Imaging, Vol. 9, K.Y. Wang, ed., 1980, pp. 275-299, Plenum, New York.

11. Kinsler, L.E., A.R. Frey, A.B. Coppens, and J.V. Sanders, Fundamentals of Acoustics, third edition, 1982, Chapter 5, Wiley, New York.

12. Jenkins, F.A., and H.E. White, Fundamentals of Physical Optics. First edition, 1937, Chapter 5, pp. 105-127, McGraw-Hill, New York.

13. Cathey, W.T., Optical Information Processing and Holography, 1974, Chapter 2, Wiley, New York.

14. Gonzalez, R.C., and P. Wintz, Digital Image Processing, 1973, Chapter 3, Addision-Wesley, Reading, MA.

15. Halliday, D., and R. Resnick, Fundamentals of Physics, 1974, Chapter 38, Revised Printing, Wiley, New York.

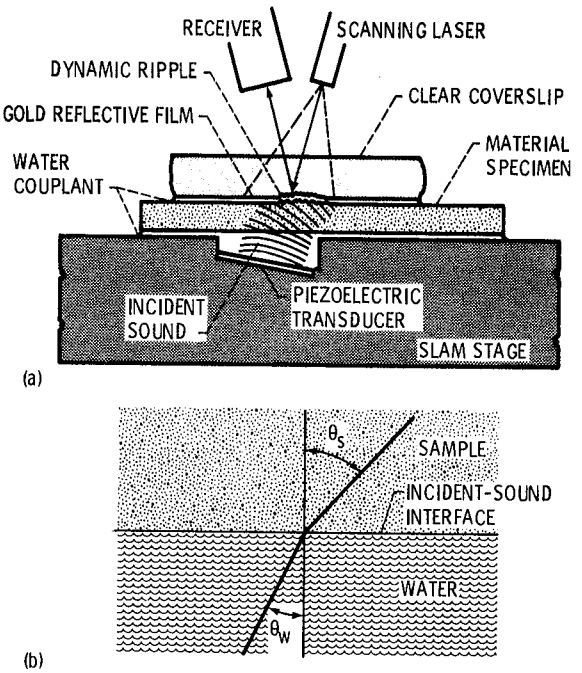

(a) General configuration used for SLAM.
(b) Schematic diagram illustrating Snell's law at incident-sound interface.

Figure 1. - Scanning laser acoustic microscopy (SLAM) technique. Ultrasound refracted at interface of water couplant and material specimen according to Snell's law.

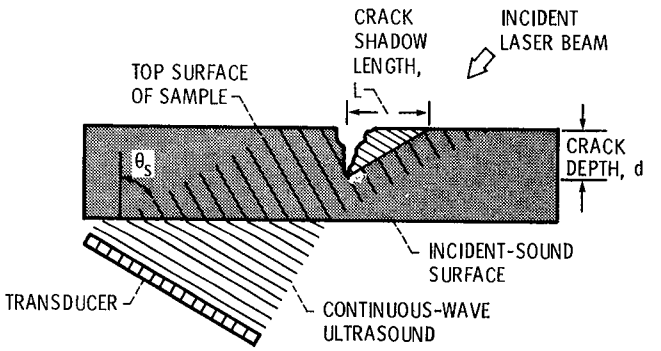

Figure 2. - Schematic diagram showing shadow region produced when ultrasound encounters crack in top surface of sample.

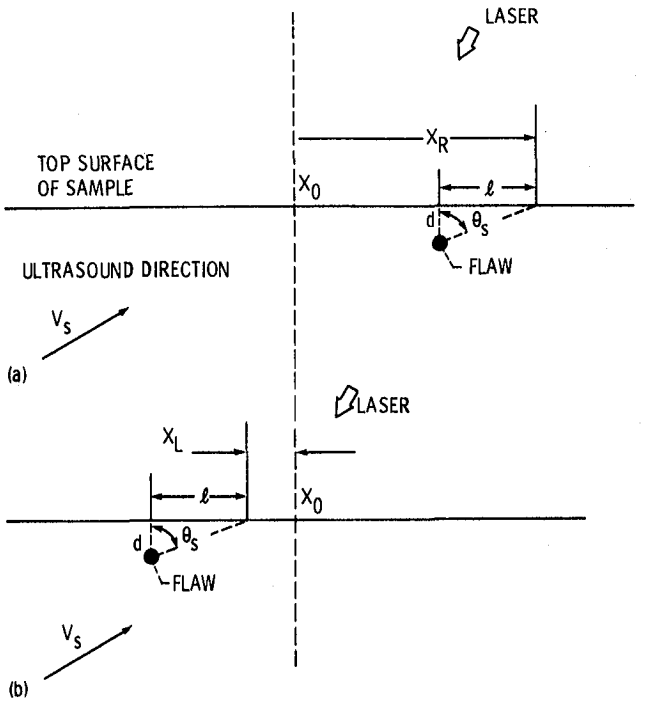

(a) Initial apparent position of flaw, X_R.
(b) Apparent position of flaw after 180^0 rotation about position X_0, X_L.

Figure 3. - Schematic diagrams showing principles of stereoscopic method used to determine depth of flaw beneath sample surface.

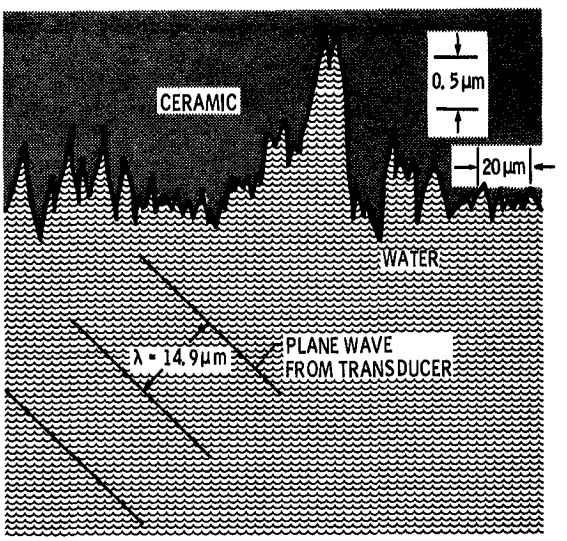

Figure 4. - Typical interface between water and ceramic sample with SLAM operating at 100 MHz. (Note magnitude of wavelength of sound in water and magnitude of topological variations on surface of ceramic specimen.)

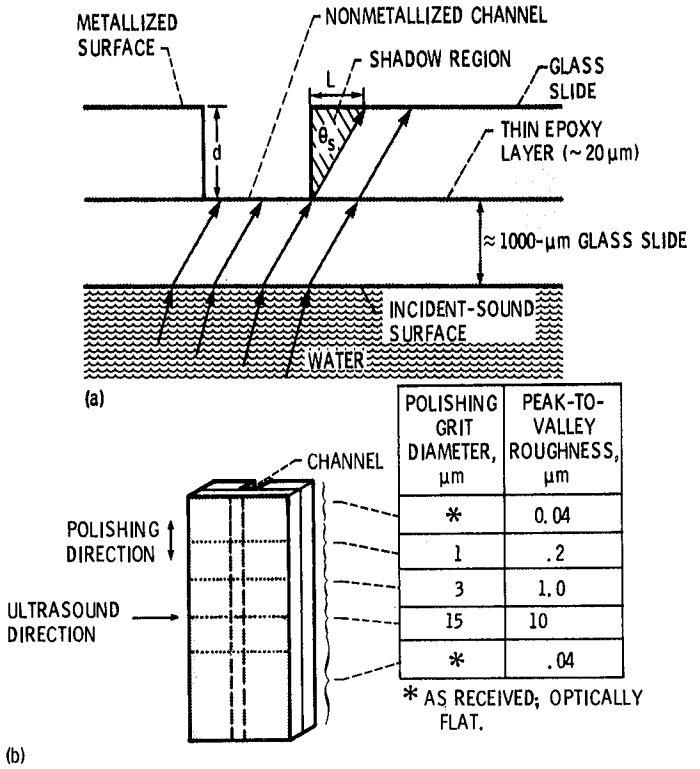

POLISHING GRIT DIAMETER, μm	PEAK-TO-VALLEY ROUGHNESS, μm
*	0.04
1	.2
3	1.0
15	10
*	.04

* AS RECEIVED; OPTICALLY FLAT.

(a) Side view of specimen showing experimental setup on SLAM with resulting shadow region.
(b) Oblique bottom view of specimen showing regions polished with 1-, 3-, and 15-μm diamond polishing paste.

Figure 5. - Glass slide specimen with artificially made channel. (Channel simulates surface crack.)

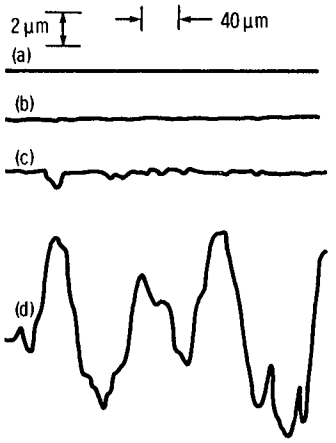

(a) Optically flat region (peak-to-valley roughness, ≤0.04 μm).
(b) Region polished with 1-μm diamond paste (peak-to-valley roughness, 0.2 μm).
(c) Region polished with 3-μm diamond paste (peak-to-valley roughness, 1 μm).
(d) Region polished with 15-μm diamond paste (peak-to-valley roughness, 10 μm).

Figure 6. - Surface profiles of regions of different surface roughnesses on glass slide.

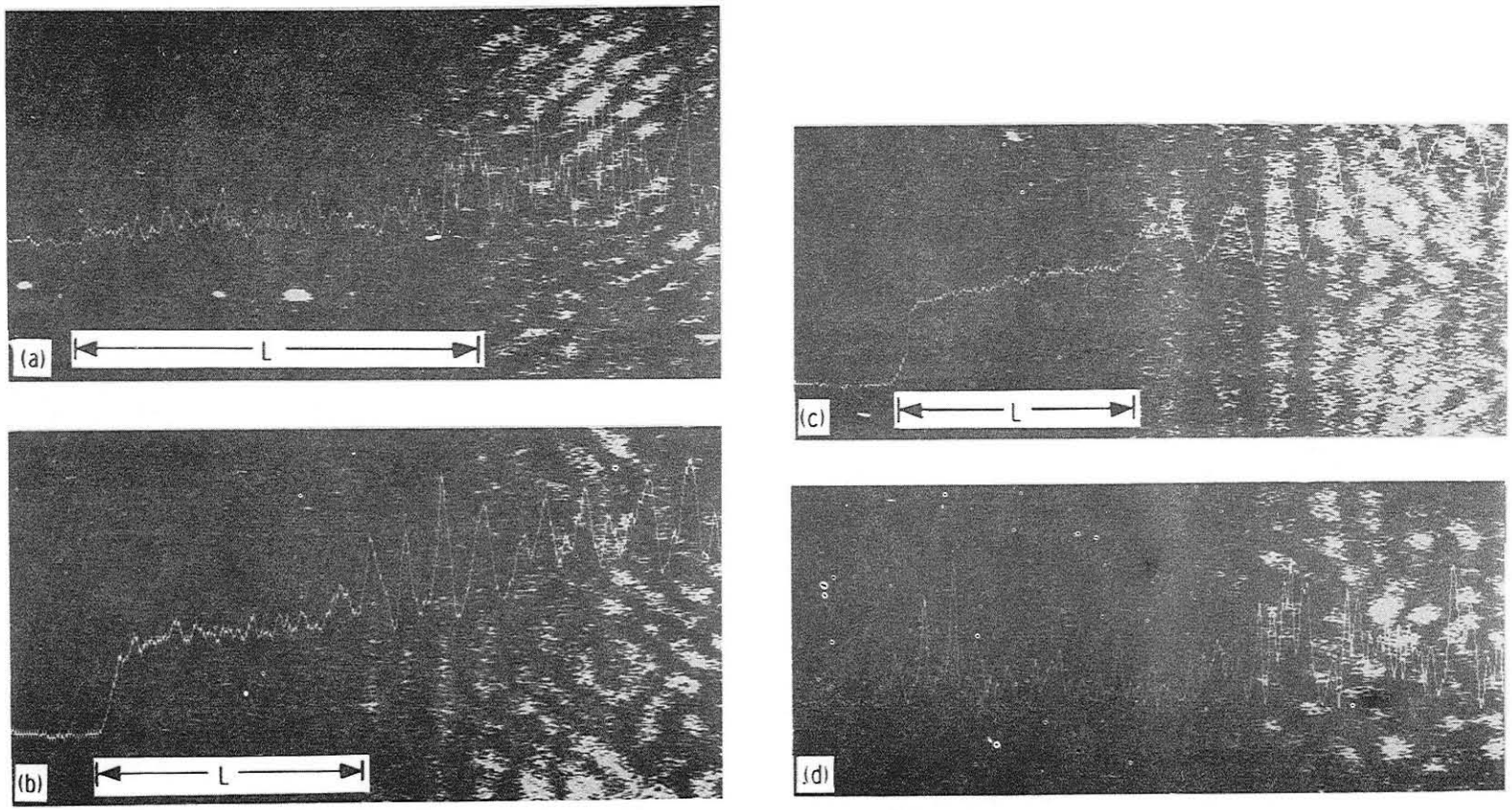

(a) Region of 0.04-μm peak-to-valley roughness.
(b) Region of 0.2-μm peak-to-valley roughness.
(c) Region of 1.0-μm peak-to-valley roughness.
(d) Region of 10-μm peak-to-valley roughness.

Figure 7. - Acoustic images of glass slide regions of different surface roughnesses. (Images taken near channel. Continuous white curves show image intensity as function of horizontal position. Shadow length L decreases with increasing surface roughness.)

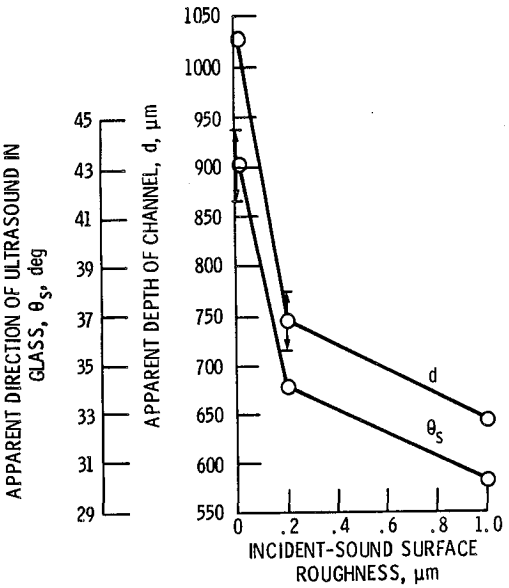

Figure 8. - Apparent depth of channel and apparent direction of ultrasound in glass as function of incident-sound surface roughness.

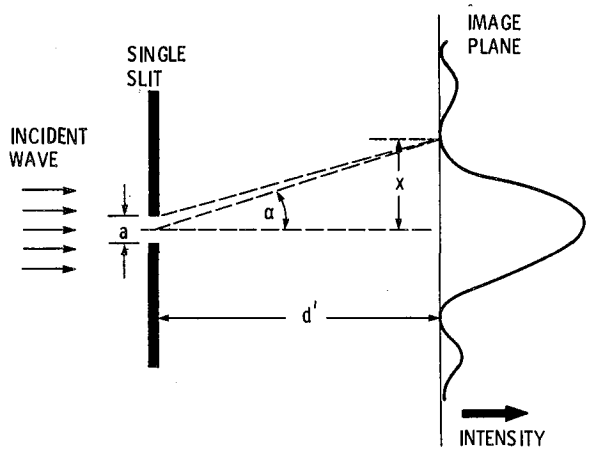

(a) Schematic diagram showing how radiation is diffracted by single slit.

Figure 9. - Diffraction of radiation from single slit under Fraunhofer conditions and Fourier transform of simulated single slit.

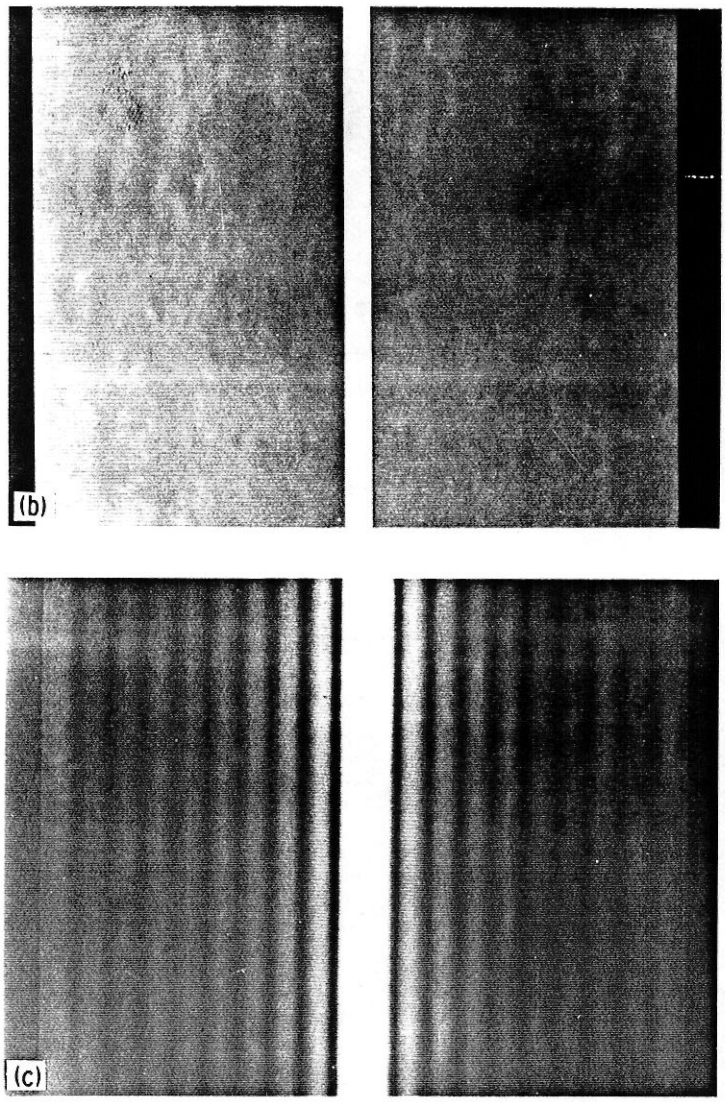

(b) Line function simulating single slit.
(c) Digital two-dimensional Fourier transform of line function.

Figure 9. - Concluded.

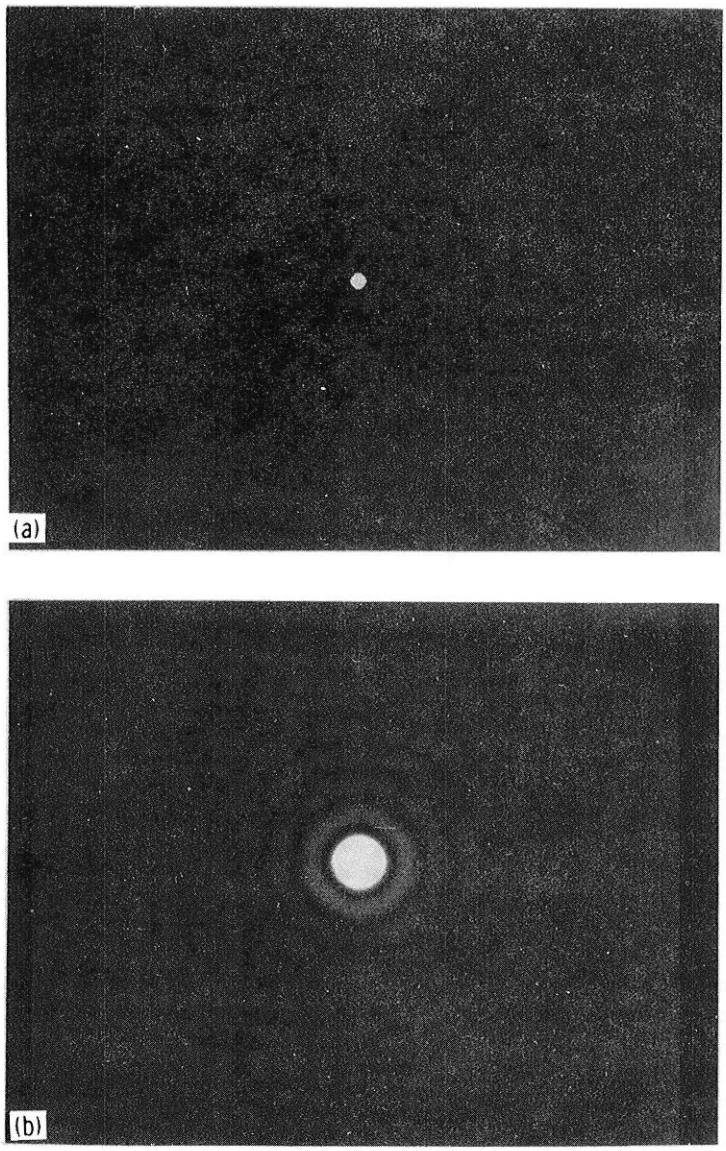

(a) Circle function simulating circular aperture.

(b) Digital two-dimensional Fourier transform of circle function.

Figure 10. - Fourier transform of simulated circular aperture.

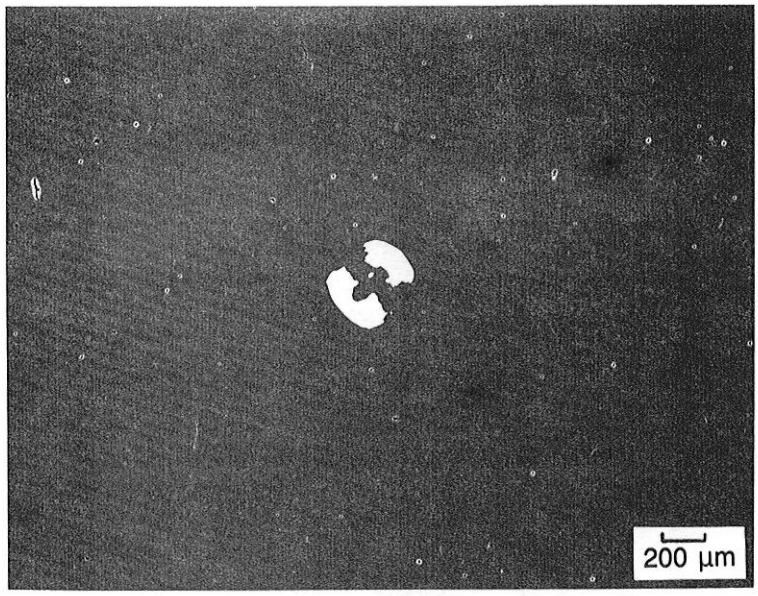

Figure 11. - Top view of subsurface spherical void occurring naturally in ordinary piece of glass, used to illustrate acoustic diffraction patterns from spherical scatterer.

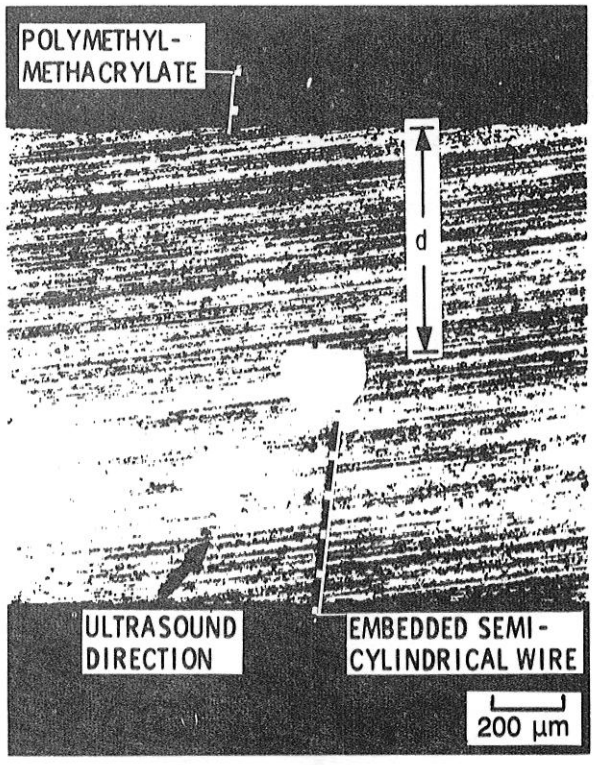

Figure 12. - Side view of tungsten wire embedded in polymethylmethacrylate slab, used to illustrate acoustic diffraction patterns from line scatterer.

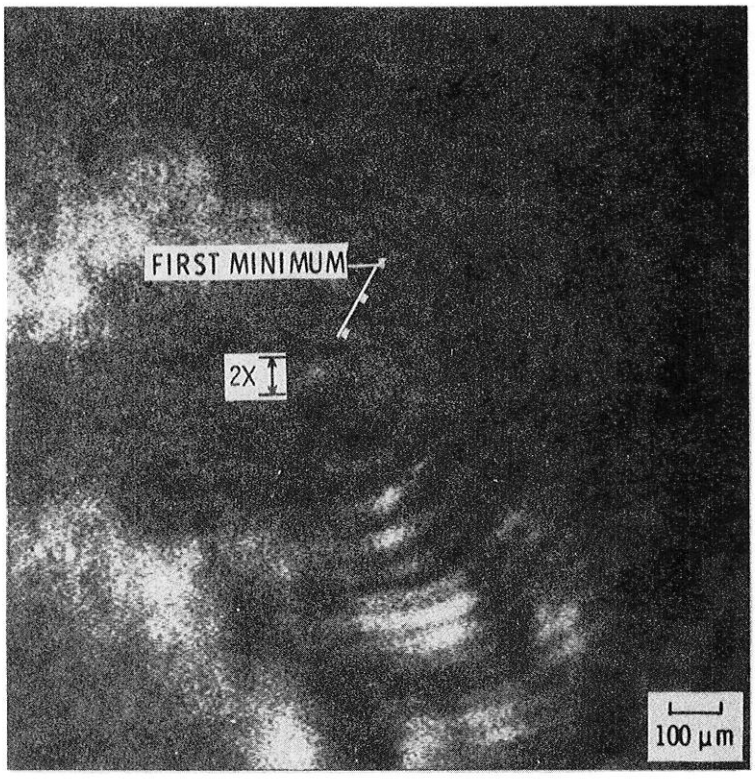

Figure 13. - Acoustic image of naturally occurring subsurface spherical void in glass (Fig. 11).

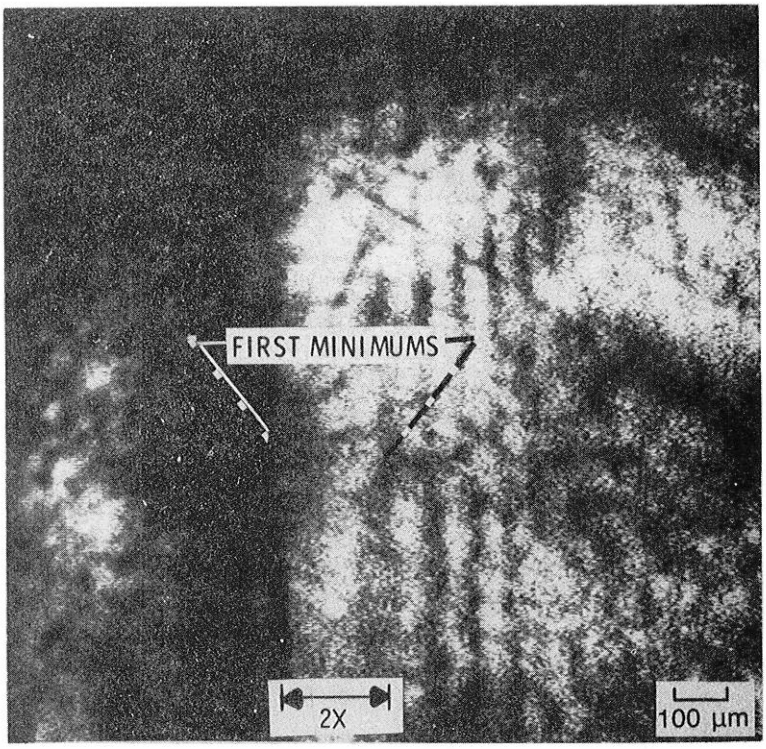

Figure 14. - Acoustic image of wire embedded in polymethylmethacrylate slab (Fig. 12).

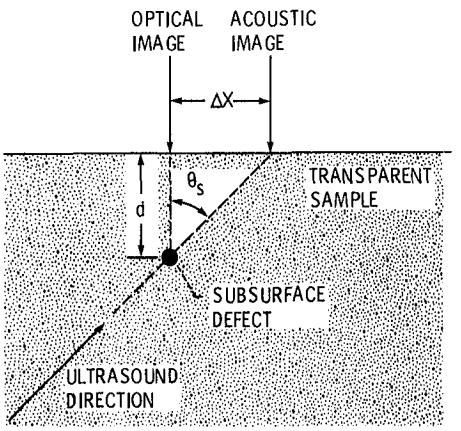

Figure 15. - Schematic diagram illustrating optical-acoustic method using SLAM for determining true ultrasound direction within material.